

## MIT Open Access Articles

*THE ACCRETION DISK CORONA AND DISK ATMOSPHERE  
OF 4U 1624-490 AS VIEWED BY THE CHANDRA-HIGH  
ENERGY TRANSMISSION GRATING SPECTROMETER*

The MIT Faculty has made this article openly available. *Please share*  
how this access benefits you. Your story matters.

**Citation:** Xiang, Jingen, Julia C. Lee, Michael A. Nowak, Jörn Wilms, and Norbert S. Schulz. “THE ACCRETION DISK CORONA AND DISK ATMOSPHERE OF 4U 1624-490 AS VIEWED BY THE CHANDRA -HIGH ENERGY TRANSMISSION GRATING SPECTROMETER .” *The Astrophysical Journal* 701, no. 2 (July 29, 2009): 984-993. © 2009 American Astronomical Society.

**As Published:** <http://dx.doi.org/10.1088/0004-637x/701/2/984>

**Publisher:** Institute of Physics/American Astronomical Society

**Persistent URL:** <http://hdl.handle.net/1721.1/96086>

**Version:** Final published version: final published article, as it appeared in a journal, conference proceedings, or other formally published context

**Terms of Use:** Article is made available in accordance with the publisher's policy and may be subject to US copyright law. Please refer to the publisher's site for terms of use.



## THE ACCRETION DISK CORONA AND DISK ATMOSPHERE OF 4U 1624–490 AS VIEWED BY THE CHANDRA-HIGH ENERGY TRANSMISSION GRATING SPECTROMETER

JINGEN XIANG<sup>1</sup>, JULIA C. LEE<sup>1</sup>, MICHAEL A. NOWAK<sup>2</sup>, JÖRN WILMS<sup>3</sup>, AND NORBERT S. SCHULZ<sup>2</sup>

<sup>1</sup> Department of Astronomy (a part of the Harvard-Smithsonian Center for Astrophysics), Harvard University, 60 Garden Street, Cambridge, MA 02138, USA; [jxiang@cfa.harvard.edu](mailto:jxiang@cfa.harvard.edu); [jlee@cfa.harvard.edu](mailto:jlee@cfa.harvard.edu)

<sup>2</sup> Massachusetts Institute of Technology, Kavli Center, 77 Massachusetts Avenue NE80, Cambridge, MA 02139, USA

<sup>3</sup> Dr. Karl-Remeis-Observatory and Erlangen Centre for Astroparticle Physics, University of Erlangen-Nuremberg, Sternwartstrasse 7, 96049 Bamberg, Germany

Received 2008 December 16; accepted 2009 May 25; published 2009 July 29

### ABSTRACT

We present a detailed spectral study (photoionization modeling and variability) of the “Big Dipper” 4U 1624–490 based on a *Chandra*-High Energy Transmission Grating Spectrometer (HETGS) observation over the  $\sim 76$  ks binary orbit of 4U 1624–490. While the continuum spectrum can be modeled using a blackbody plus power law, a slightly better fit is obtained using a single  $\Gamma = 2.25$  power-law partially (71%) covered by a local absorber of column density  $N_{\text{H, Local}} = 8.1_{-0.6}^{+0.7} \times 10^{22} \text{ cm}^{-2}$ . The data show a possible quasi-sinusoidal modulation with period  $43_{-9}^{+13}$  ks that might be due to changes in local obscuration. Photoionization modeling with the *XSTAR* code and variability studies of the observed strong Fe xxv and Fe xxvi absorption lines point to a two-temperature plasma for their origin: a highly ionized component of ionization parameter  $\xi_{\text{hot}} \approx 10^{4.3} \text{ erg cm s}^{-1}$  ( $T \sim 3.0 \times 10^6$  K) associated with an extended accretion disk corona of radius  $R \sim 3 \times 10^{10}$  cm, and a less-ionized more variable component of  $\xi \approx 10^{3.4} \text{ erg cm s}^{-1}$  ( $T \sim 1.0 \times 10^6$  K) and  $\xi \approx 10^{3.1} \text{ erg cm s}^{-1}$  ( $T \sim 0.9 \times 10^6$  K) coincident with the accretion disk rim. We use this, with the observed Fe xxv and Fe xxvi absorption line variations (in wavelength, strength, and width) to construct a viewing geometry that is mapped to changes in plasma conditions over the 4U 1624–490 orbital period.

*Key words:* accretion, accretion disks – plasmas – X-rays: binaries – X-rays: individual (4U 1624–490)

### 1. INTRODUCTION

The “Big Dipper” 4U 1624–490, with its high energy ( $> 8$  keV) flaring between dips, is one of the most “extreme” of the dipping sources. Its nickname derives in part from the fact that it has one of the longest orbital periods (21 hr  $\approx 76$  ks; Jones & Watson 1989) and dips that last  $\approx 2.7$  hr  $\approx 11$  ks (Watson et al. 1985; Balucińska-Church et al. 2000). The prevailing idea for explaining this behavior is that the dips are likely due to obscuration by a raised accretion disk rim at the location where the infalling accretion stream impacts the disk. By accounting for the quasi-steady X-ray dust scattering halo, one can show that obscuration during dips is  $> 90\%$  (Xiang et al. 2007; Iaria et al. 2007). The dips exhibit broad, shallow shoulders, with a rapid ingress/egress to the deepest dip levels. A point-like soft X-ray source reasonably can be inferred from the rapid ingress/egress and dip variability. While the dipping seems to saturate at a minimum level, rapid ( $< 30$  s), short duration, large amplitude spikes are seen. This behavior argues for the obscuring medium having a well defined boundary, but a highly variable, erratic covering.

Since its discovery (Watson et al. 1985), 4U 1624–490 has been studied extensively with X-ray telescopes including *EXOSAT* (Church & Balucińska-Church 1995), *Ginga* (Jones & Watson 1989), *Einstein* (Christian & Swank 1997), *ASCA* (Angelini et al. 1997; Asai et al. 2000), *BeppoSAX* (Balucińska-Church et al. 2000), *RXTE* (Balucińska-Church et al. 2001; Lommen et al. 2005; Smale et al. 2001), *XMM-Newton* (Parmar et al. 2002; Díaz-Trigo et al. 2006), and *Chandra* (Iaria et al. 2007; Xiang et al. 2007; Wachter et al. 2005). From these studies we know that 4U 1624–490 is highly absorbed, both extrinsically and intrinsically. Models have been developed over the years wherein the spectrum consists of the following: large external absorption, a scattering halo, a point-like (i.e., rapidly

absorbed) blackbody, and an extended (i.e., partially absorbed) accretion disk corona (ADC; Balucińska-Church et al. 2000, 2001; Smale et al. 2001). Observations also have revealed a broad Fe  $K\alpha$  emission line (Smale et al. 2001; Parmar et al. 2002). It is therefore likely that we are viewing both the inner (point-like source, broad lines) and outer (dips, variable absorption) accretion disk regions in this highly inclined, high-Eddington fraction, low-mass X-ray binary (LMXB).

From the point of view of high-resolution *Chandra* spectroscopy, 4U 1624–490 may be in many ways analogous to the bright, highly inclined, variable, and absorbed microquasar GRS 1915+105 (Lee et al. 2002; Neilsen & Lee 2009). As such, there are key questions concerning the physical environment of 4U 1624–490 that only high-resolution X-ray spectroscopy can address. Is the extended corona a photoionized atmosphere in equilibrium? Medium-resolution *XMM-Newton* EPIC data provide some clues. Parmar et al. (2002) identified “narrow” ( $< 50$  eV) resonant absorption lines from Fe xxvi Ly $\alpha$ , Fe xxvi He  $\alpha$ , and a broad(er) 470 eV Fe  $K\alpha$  emission line (see also Smale et al. 2001). Like all X-ray sensitive CCD cameras, however, the *XMM-Newton* EPIC, with a resolution comparable to the *ASCA* Solid-State Imaging Spectrometer (SIS), is fundamentally limited in the extent to which it can resolve such features. A recent analysis of these *Chandra* grating observations by Iaria et al. (2007), while providing a better measurement of the ionized Fe lines given the better HEG resolution compared with EPIC in this spectral band, did not undertake the in-depth modeling necessary to describe the viewing geometry for the photoionized gas. Furthermore, based on the analysis presented in this paper, we offer an alternative scenario to the interpretation of Iaria et al. that the observed absorption line width can be attributed to bulk Comptonization.

As a prelude to this paper, we studied the dust scattering halo properties of 4U 1624–490 with this *Chandra*-High

Energy Transmission Grating Spectrometer (HETGS) observation in an attempt to first better understand the distribution of intervening line-of-sight material (size and spatial distribution of dust grains), which we found to be heterogeneously distributed near the source and in the spiral arms of the Galaxy (Xiang et al. 2007). Additionally, by measuring scattering delay times as a function of angular distance in comparison to the 4U 1624–490 source light curve, we were able to obtain a much more accurate distance measurement of  $15^{+2.9}_{-2.6}$  kpc to 4U 1624–490. In this paper, we use the same *Chandra*-HETGS observation to focus on the binary properties with an in-depth analysis of the HETGS spectra. (These are the same data published by Iaria et al. (2007).) Specifically, we explore the persistent-phase spectrum over the 4U 1624–490 orbital period in the context of Section 2.1: photoionization modeling using *XSTAR* (Kallman 2005, ver. 2.1kn7), and Section 2.2: detailed variability studies of the detected ionized Fe xxv and Fe xxvi absorption lines and continuum. In particular, we study the orbital phase evolution of the detected absorption lines as a function of the time periods immediately before and after (Section 2.2.1), as well as near to and far from the dipping events (Section 2.2.2), in addition to an analysis of the short-duration ( $\approx 10$  ks) absorption changes over the 4U 1624–490  $\approx 21$  hr orbital period. The results are summarized and discussed in Section 3 in the context of a simple two temperature absorber model, and we specifically focus on the quasi-sinusoidal modulation of these plasma components, as well as modulation of the continuum components, over the binary orbital period.

## 2. OBSERVATIONS AND DATA ANALYSIS

We observed 4U 1624–490 with the *Chandra*-HETGS (Canizares et al. 2005) in time graded mode beginning at 06:26:06 UT on 2004 June 04 (MJD 53160.26813, Obs. ID: 4559), covering one binary orbit of  $\approx 76$  ks. Given that 4U 1624–490 is bright ( $\approx 50$  mCrab; Smale et al. 2001; Díaz-Trigo et al. 2006), we mitigate pileup and telemetry problems by using a one-half subarray of 512 columns per CCD in order to reduce the frame time to 1.7 s from the nominal 3.2 s. Despite these efforts, the zeroth-order ACIS-S data are heavily piled-up, rendering difficult the drawing of useful conclusions from the zeroth-order spectrum. Accordingly, this paper focuses only on spectral and light curve analysis of the HETGS grating spectra.

We use CIAO 3.4 with CALDB 3.3 for our data reduction efforts. In order to ensure the most accurate wavelength measurements possible for this observation, we calculate the exact zeroth-order position using a code that fits the intersection of the dispersed MEG data with the zeroth-order “readout trace” on the ACIS-S3 chip.<sup>4</sup> Using this technique it is expected the accuracy of the zeroth-order position is better than 0.1 detector pixels, translating to a wavelength accuracy of 0.001 Å (corresponding to  $164 \text{ km s}^{-1}$  at 6.8 keV) for both the High Energy Grating (HEG) and Medium Energy Grating (MEG) first orders. Positive and negative first-order spectra for HEG and MEG were combined for analysis.

For our analysis, we generate first-order time-averaged HEG and MEG spectra spanning the non-dip phases of the full 76 ks orbital period (resulting in  $\approx 67$  ks of usable data) to study the properties of the persistent phase continuum spectrum and to look for faint lines (Section 2.1). We also generate phase-dependent spectra (labeled “a–g,” and combinations thereof, as indicated by the light curve in Figure 1) to study the time

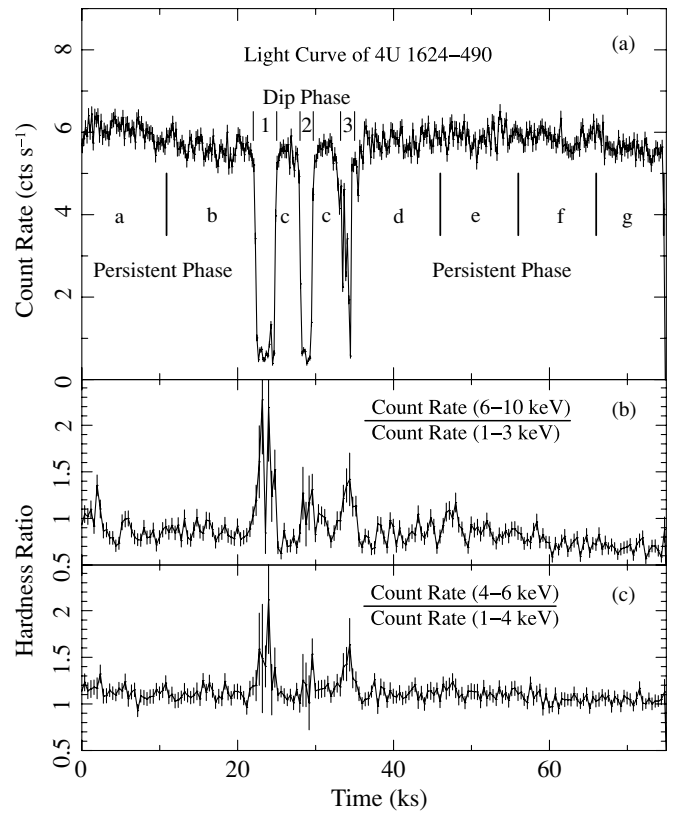


**Figure 1.** (a) First-order 1–10 keV HEG+MEG light curve of 4U 1624–490, and (b) and (c) associated hardness ratios that reveal spectral hardening during the dip periods. Throughout the paper, time zero corresponds to MJD 53160.3.

evolution of the plasma via observed changes in the line profiles and fluxes (Section 2.2). Figure 1 also shows that our observation encompasses  $\approx 9.7$  ks ( $\approx 2.7$  hr; sum of dip phases 1+2+3) worth of occulted periods. The longest duration of an individual dip is seen to be  $\approx 3.5$  ks and the largest occultation is  $\approx 90\%$ . Possibly because of the low energy absorption, the spectrum is seen to harden during dipping periods. We are unable to extract useful information from the *dip-phase* HETGS spectrum due to the low counts.

### 2.1. The Average Persistent Phase Spectrum

As a prelude to spectral analysis, we first determined pileup fraction (defined to be the fraction of frames that have detected events containing two or more events per frame per pixel) in the first-order grating spectra. Since pileup is dependent on the count rate in each CCD pixel, we use the count rate in the HEG  $\pm 1$  and MEG  $\pm 1$  spectra for our estimates. We find that the maximal pileup fraction of HEG +1 and –1 order spectra is  $\approx 1.0\%$  at  $\approx 2.5$  Å ( $\approx 5$  keV). Similarly MEG +1 and –1 order spectra are piled up at less than  $\approx 1.0\%$  except for the range 2.5–3.5 Å (3.5–5.0 keV) where the maximal pileup fraction reaches  $\approx 2.0\%$ . Accordingly, we ignore regions of the spectrum with pileup  $> 1\%$ . As such, we fit only to 1.2–7.3 Å (1.7–10.0 keV) HEG spectra, and MEG spectra over the 1.5–2.5 Å (1.7–3.5 keV) and 3.5–7.5 Å (5.0–8.0 keV) range. The spectra are rebinned to satisfy a signal-to-noise ratio (S/N)  $> 5$  and  $0.005$  Å per bin for the HEG first order, S/N  $> 5$  and  $0.01$  Å per bin for the MEG first-order, respectively. ISIS<sup>5</sup> (Houck & Denicola 2000; Noble & Nowak 2008) was used as the fitting engine for our analysis.

<sup>4</sup> <http://space.mit.edu/cxc/analysis/findzo/>

<sup>5</sup> <http://space.mit.edu/cxc/isis/>

**Table 1**  
Best-fit Continuum and Broad Fe Emission Line Parameters

Component	Parameter	Persistent	Pre-dip	Post-dip	Near-dip	Far-dip
	$\chi^2/\text{dof}$	1435/1338	1003/992	1205/1162	1026/1066	1248/1194
	$L_X$ (erg s $^{-1}$ )	$4.9 \times 10^{37}$	$4.8 \times 10^{37}$	$5.0 \times 10^{37}$	$4.6 \times 10^{37}$	$4.9 \times 10^{37}$
TBABS <sup>a</sup>	$N_H$ ( $10^{22}$ cm $^{-2}$ )	$7.6^{+0.4}_{-0.4}$	$7.4^{+0.6}_{-0.4}$	$7.8^{+0.5}_{-0.5}$	$7.5^{+0.6}_{-0.5}$	$7.6^{+0.4}_{-0.4}$
Blackbody	kT (keV)	$1.39^{+0.05}_{-0.04}$	$1.38^{+0.08}_{-0.05}$	$1.43^{+0.06}_{-0.05}$	$1.43^{+0.08}_{-0.06}$	$1.35^{+0.06}_{-0.04}$
	Norm ( $10^{-2}$ )	$1.42^{+0.15}_{-0.11}$	$1.52^{+0.46}_{-0.29}$	$1.53^{+0.14}_{-0.12}$	$1.45^{+0.27}_{-0.16}$	$1.41^{+0.24}_{-0.15}$
Power law	$\Gamma$	$1.14^{+0.33}_{-0.48}$	$0.65^{+0.64}_{-1.70}$	$1.43^{+0.43}_{-0.55}$	$1.13^{+0.54}_{-1.17}$	$1.06^{+0.39}_{-0.71}$
	Norm ( $10^{-2}$ ph cm $^{-2}$ s $^{-1}$ keV $^{-1}$ )	$6.2^{+5.8}_{-4.1}$	$2.7^{+8.3}_{-2.6}$	$9.1^{+9.9}_{-6.4}$	$5.1^{+8.8}_{-4.7}$	$5.8^{+7.2}_{-4.7}$
Fe emission feature	$E_{\text{Fe}}$ (keV)	$6.76^{+0.20}_{-0.17}$	$6.57^{+0.19}_{-0.19}$	$6.66^{+0.30}_{-0.08}$	$6.97^{+0.47}_{-0.31}$	$6.68^{+0.07}_{-0.07}$
	(1.83 Å)	(1.83 Å)	(1.89 Å)	(1.86 Å)	(1.78 Å)	(1.86 Å)
	Flux $I_{\text{Fe}}$ ( $10^{-3}$ ph cm $^{-2}$ s $^{-1}$ )	$0.9^{+0.4}_{-0.3}$	$0.8^{+0.5}_{-0.4}$	$0.6^{+0.4}_{-0.3}$	$1.2^{+0.6}_{-0.6}$	$0.8^{+0.2}_{-0.2}$
	Width $\sigma$ (keV)	$0.34^{+0.19}_{-0.14}$	$0.24^{+0.19}_{-0.12}$	$0.13^{+0.30}_{-0.07}$	$0.50^{+0.32}_{-0.15}$	$0.18^{+0.07}_{-0.05}$
	( $10^3$ km s $^{-1}$ )	( $15^{+8}_{-6}$ )	( $11^{+9}_{-6}$ )	( $6^{+14}_{-3}$ )	( $22^{+14}_{-7}$ )	( $8^{+3}_{-2}$ )

**Note.** <sup>a</sup> TBABS is the absorption model described in Section 2.1.1. Errors are quoted at 90% confidence.

### 2.1.1. Broadband Continuum

The 4U 1624–490 broadband continuum as determined from the HEG spectrum has already been discussed at length in our previous paper focusing on the scattering halo associated with this source (Xiang et al. 2007). The inclusion of the MEG spectrum to our fitting here gives consistent results for a blackbody + power-law continuum modified by absorption from neutral material ( $N_H$ ). These parameters are listed in column 3 of Table 1, and a spectrum is shown in Figure 2. In our previous work, however, we were concerned by the fact that our best-fit parameters were noticeably different from that published by Iaria et al. (2007) for the same data set. In particular, our best-fit photon index  $\Gamma = 1.14^{+0.33}_{-0.48}$  is slightly harder than the  $\Gamma = 2.0^{+0.30}_{-0.55}$  noted by Iaria et al. A cursory check showed that the difference had very little to do with absorption models, e.g.,  $\Gamma \approx 1.4$  for PHABS (Balucińska-Church & McCammon 1992), versus  $\Gamma \approx 1.2$  for TBABS, which use the updated cross-sections and abundances of Wilms et al. (2000), fitting tools (e.g., ISIS vs. XSPEC; Arnaud 1996), binning, or choice of fitted spectral regions. For completeness, we also looked into calibration effects and find that at least some of the differences had to do with a difference between CALDB 3.2 (used by Iaria et al.) versus CALDB 3.3 (this paper). A reduction of the 4U 1624–490 spectra using CALDB 3.2 resulted in a slightly softer power law ( $\Gamma \approx 1.8$ ), compared with our CALDB 3.3 value of  $\Gamma \approx 1.4$  (PHABS). Even though the CALDB 3.2 measure of photon index is closer to the  $\Gamma = 2.0^{+0.30}_{-0.55}$  value quoted by Iaria et al. for this data set, a full agreement with the values of Iaria et al. is not reached even when trying to reproduce every step of their analysis process. We can only speculate that a combination of effects, including new reprocessing that accounts for afterglow events, and the careful treatment of pileup incorporated here may be responsible for the rest of the discrepancy. We also note that our photon index is slightly harder than the values of  $\Gamma = 2.0^{+0.5}_{-0.8}$  for a *BeppoSAX* observation by Balucińska-Church et al. (2000) and  $\Gamma = 2.02 \pm 0.12$  for a *XMM-Newton* observation by Parmar et al. (2002). The difference is possibly caused by the different luminosity states (see the next paragraph) or by the limited *Chandra*-HETGS band coverage (e.g., 0.5–10 keV) and the severe absorption at the low energies coupled with limited counts at the high energies.

Based upon our best-fit continuum, the 0.6–10 keV flux of 4U 1624–490 is  $\approx 1.07 \times 10^{-9}$  erg cm $^{-2}$  s $^{-1}$  ( $\approx 50$  mCrab), corresponding to an unabsorbed 0.6–10 keV luminosity of

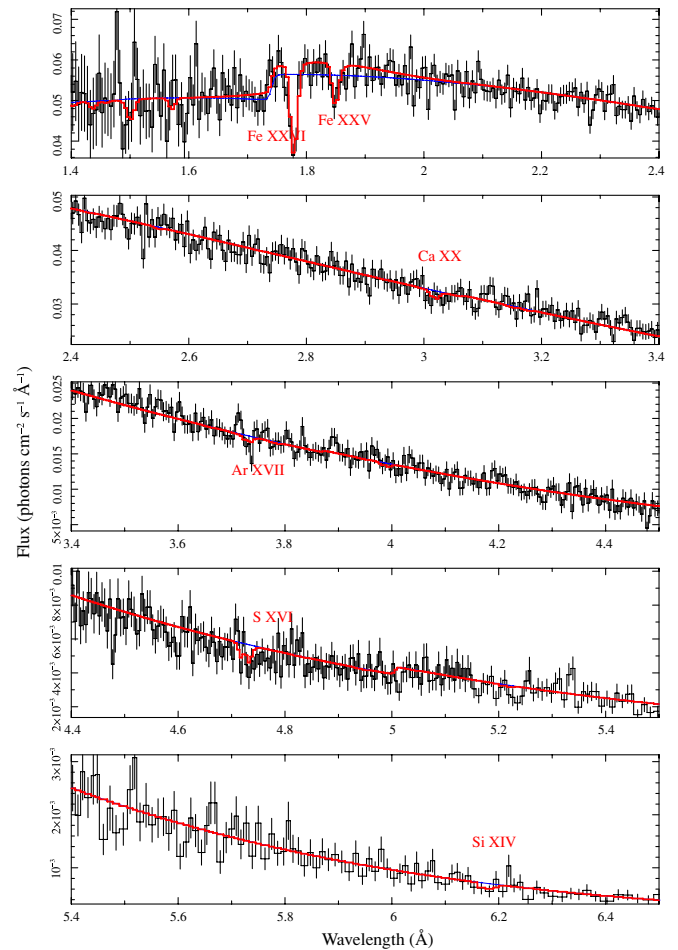


**Figure 2.** Best-fit persistent phase continuum and broad Fe emission line model (red) of Table 1 modified by two photoionized absorption lines (see Section 2.1.3) overlaid on the time-averaged HEG first-order spectrum of 4U 1624–490 over its  $\approx 76$  ks orbital period. The blue line is the best-fit model excluding the Fe emission line and the ionized absorption lines.

$\approx 4.9 \times 10^{37}$  erg s $^{-1}$  (assuming a distance of 15.0 kpc as determined from our scattering halo analysis; Xiang et al. 2007). The luminosity is similar to that observed with *XMM-Newton* (Parmar et al. 2002) but significantly lower than that using the *RXTE* (Smale et al. 2001) and *EXOSAT* (Church & Balucińska-Church 1995) observations. As discussed by Smale et al. (2001), the luminosity during different observations can



change significantly and thus the emission parameters should not necessarily be expected to be completely consistent.

As an alternative to the continuum model of a blackbody plus power law, we also considered a continuum consisting solely of a partially covered power law. In this model, the soft excess that had been described by the blackbody is now modeled by the soft end of the uncovered power law. Specifically, the model is given by

$$f_{\text{obs}}(E) = A e^{-N_{\text{H, LOS}} \sigma_{\text{ph}}(E)} (1 - x + x e^{-N_{\text{H, Local}} \sigma_{\text{ph}}(E)}) E^{-\Gamma}, \quad (1)$$

where  $N_{\text{H, LOS}}$  is the equivalent hydrogen column along the line of sight,  $N_{\text{H, Local}}$  is the equivalent hydrogen column local to the system,  $A$  is the normalization of the power-law continuum, and  $x$  is the partial covering fraction. We find that this model ( $\chi^2/\text{dof} = 1413/1338$ ) describes the persistent phase spectrum slightly better than the blackbody plus power-law model ( $\chi^2/\text{dof} = 1435/1338$ ), and yields values of  $x = (71 \pm 3)\%$ ,  $\Gamma = 2.25 \pm 0.06$ , and  $N_{\text{H, Local}} = 8.1_{-0.6}^{+0.7} \times 10^{22} \text{ cm}^{-2}$ . Again, as discussed above, the limited *Chandra*-HETGS band coverage (e.g., 0.5–10 keV) and the limited counts at high energies do not allow us to distinguish between these two models for the time-averaged spectra. Thus for some of the results that follow, e.g., the modeling of the broad emission line (Section 2.1.2) and narrow ionized absorption lines (Section 2.1.3), the results are insensitive to which the continuum model that we choose. As we elaborate upon in the discussion of short timescale changes (Section 2.2.3), however, the partial covering model may more naturally explain spectral variations associated with the source’s light curve.

### 2.1.2. Broad Emission Line

A significant and broad excess around 6.6 keV was found when we checked the fit residuals in both the HEG and MEG spectra. We also saw deficits around 6.7 keV and 7.0 keV corresponding to narrow absorption lines. These are discussed in more detail in Sections 2.1.3 and 2.2. The broad excess has been identified with Fe K emission typically detected in LMXBs (first significant detection: Suzuki et al. 1984 with *Tenma*; with *EXOSAT*, White et al. 1986; Hirano et al. 1987; Asai et al. 2000 for an *ASCA* study of 20 LMXBs, including 4U 1624–490). Asai et al. (2000) postulated that the line is likely produced through the radiative recombination in a photoionized plasma and that its broad width is attributable to a confluence of processes in the ADC, including Compton scattering and Doppler shifts arising from Keplerian motions. Parmar et al. (2002) also studied the broad emission line from 4U 1624–490 with *XMM-Newton*, and found that the best-fit energy for the emission line depends on whether or not the Fe absorption lines were also modeled. When the absorption lines were included, Parmar et al. found a best-fit emission energy of  $6.58_{-0.04}^{+0.07}$  keV in contrast to the  $6.39_{-0.04}^{+0.03}$  keV value found when the absorption features were excluded. The HEG clearly shows strong Fe xxv and Fe xxvi absorption lines in our HEG spectrum, which are therefore included in our modeling of the broad emission feature. The continuum model is the blackbody plus power-law model of Section 2.1.1.

Like the persistent phase spectrum, the far-dip (a+e+f+g;  $\approx 39$  ks) and near-dip (b+c+d;  $\approx 29$  ks) spectra of Figure 3 reveal a broad emission line with a best-fit energy that is most consistent with He-like Fe xxv at  $\approx 6.7$  keV (Table 1). It is interesting to note that the peak energy for the broad emission feature in the near-dip phase spectrum points to even higher

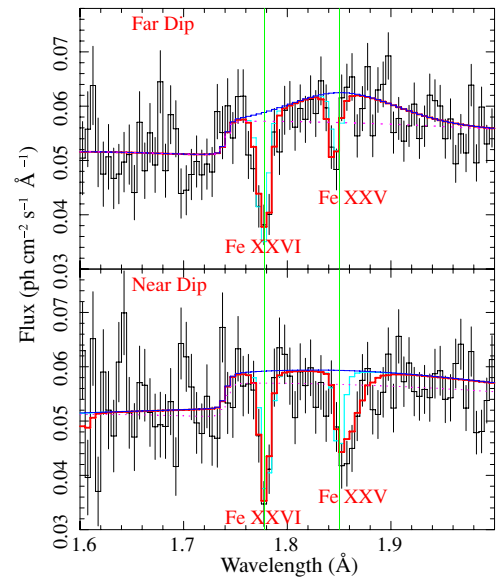


**Figure 3.** Fluxed spectra (black) and best-fit two-component ionization model (red) of Section 2.2.2 during the far-dip (top) and near-dip (bottom) 4U 1624–490 phases. Represented in light blue is a single-component ionization model that clearly fits the data less well, in dark blue is the model excluding the ionized absorption lines. Vertical green lines indicate the laboratory wavelengths of Fe xxv (1.850 Å) and Fe xxvi (1.778 Å).

ionization H-like Fe xxvi and to a broader velocity width, although the uncertainties of the modeling do not allow us to make any strong claims to this effect. If real, it would be of interest to consider whether Compton scattering can be a mechanism for line broadening in LMXBs as suggested by Asai et al. (2000). Note that the highest values for the fitted line width,  $\approx 0.5$  keV, correspond to velocities that if associated with the accretion disk arise at radii  $> 100 \text{ GM}/c^2$ . Thus, the broad emission line is not necessarily cospatial with the blackbody component, if indeed a blackbody+power law is the better description of the true, underlying physical description of the observed spectra. The presence of a broad line therefore does not provide us with a means of distinguishing between the blackbody+power law and partially covered power-law models for the continuum spectra, and could be consistent with either model.

### 2.1.3. Photoionization Modeling of the Narrow Ionized Absorption Lines

The three most obvious absorption lines that show up in the *Chandra*-HETGS spectra (Fe xxvi at  $\approx 7.0$  keV/1.778 Å, Fe xxv at  $\approx 6.7$  keV/1.850 Å, and Ca xx at  $\approx 4.1$  keV/3.020 Å; see Figure 2) have already been reported by Iaria et al., albeit based upon Gaussian fits to these data, as opposed to the modeling with photoionization codes as we present in this work. Ionized absorption lines were initially discovered for 4U 1624–490 in *XMM-Newton* EPIC data (Parmar et al. 2002). Here, for the time-averaged spectra we go beyond previous studies by modeling the absorption spectrum of 4U 1624–490 using an analytic version of *XSTAR* v2.1ln2 (Kallman 2005). For these *XSTAR* fits, the column density, ionization, turbulent velocity width, and velocity shift were allowed to vary. The abundance of elements from C to Fe were fixed at solar values (Grevesse et al. 1996), although subsequent fits that allowed these parameters to vary gave abundance results similar to solar values within 90% confidence errors. If

**Table 2**  
Ions Predicted from XSTAR Fit to Time-averaged Spectrum

Ion	Transition	$f_{ij}^a$	$\lambda_{\text{lab}}^b$	$\lambda_{\text{obs}}^c$	$\tau^d$	$W_\lambda^e$	Model <sup>f</sup>	Comments
Mg XII	Ly $\beta$ : $1s^2S_{1/2} \rightarrow 3p(^2P^o)$	0.079	7.106	7.111	6.75	0.51	w2	Weak
Si XIV	Ly $\alpha$ : $1s^2S_{1/2} \rightarrow 2p(^2P^o)$	0.414	6.182	6.170	5.45	1.10	w1	Weak
				6.186	81.70	4.10	w2	Strong
Si XIV	Ly $\beta$ : $1s^2S_{1/2} \rightarrow 3p(^2P^o)$	0.079	5.217	5.221	13.70	0.70	w2	Weak
S XVI	Ly $\alpha$ : $1s^2S_{1/2} \rightarrow 2p(^2P^o)$	0.413	4.729	4.720	6.31	0.98	w1	Weak
				4.732	83.00	3.20	w2	Strong
S XVI	Ly $\beta$ : $1s^2S_{1/2} \rightarrow 3p(^2P^o)$	0.079	3.991	3.994	14.20	0.58	w2	Weak
Ar XVIII	Ly $\alpha$ : $1s^2S_{1/2} \rightarrow 2p(^2P^o)$	0.412	3.733	3.736	22.50	0.79	w2	Weak
Ca XX	Ly $\alpha$ : $1s^2S_{1/2} \rightarrow 2p(^2P^o)$	0.411	3.020	3.022	12.00	0.62	w2	Weak
Fe XXV	He $\alpha$ : $1s^2(^1S_0) \rightarrow 1s2p(^1P_1^o)$	0.775	1.850	1.851	113.00	2.30	w2	Strong
Fe XXV	He $\beta$ : $1s^2(^1S_0) \rightarrow 1s3p(^1P_1^o)$	0.152	1.573	1.574	31.00	0.74	w2	Weak
Fe XXVI	Ly $\alpha$ : $1s^2S_{1/2} \rightarrow 2p(^2P^o)$	0.408	1.780	1.776	103.00	4.00	w1	Strong
				1.781	145.00	2.10	w2	Strong
Fe XXVI	Ly $\beta$ : $1s^2S_{1/2} \rightarrow 3p(^2P^o)$	0.078	1.503	1.500	12.70	0.72	w1	Weak
				1.504	29.60	0.65	w2	Weak
Fe XXVI	Ly $\gamma$ : $1s^2S_{1/2} \rightarrow 4p(^2P^o)$	0.029	1.438	1.435	5.14	0.26	w1	Weak
				1.439	10.90	0.26	w2	Weak
Fe XXVI	Ly $\delta$ : $1s^2S_{1/2} \rightarrow 5p(^2P^o)$	0.014	1.404	1.401	2.65	0.12	w1	Weak
				1.405	3.77	0.13	w2	Weak

**Notes.**

<sup>a</sup> Oscillator strength.

<sup>b</sup> Laboratory wavelength.

<sup>c</sup> Observed wavelength.

<sup>d</sup> Optical depth.

<sup>e</sup> Equivalent width.

<sup>f</sup> “w1” and “w2” refer to the absorber-1 and absorber-2, respectively.

we adopt the interpretation of Iaria et al. and consider a one-zone plasma, the time-averaged spectrum over the course of the 4U 1624–490 orbital period can be modeled reasonably well with a hot plasma of  $\log \xi = 3.6 \pm 0.2$  ionizing a column of  $\log N_{\text{H}} = 22.53_{-0.08}^{+0.07} \text{ cm}^{-2}$ , with turbulent velocities of  $v_{\text{turb}} = 656_{-334}^{+480} \text{ km s}^{-1}$ . Because our variability analysis of Section 2.2 strongly points to a two-ionization zone model for the 4U 1624–490 absorbers, we describe our model for the time-averaged spectrum accordingly. For this model, a combination of ionized absorber-1 ( $\log \xi = 4.3 \pm 0.4$ ;  $\log N_{\text{H}} = 23.3 \pm 0.2$ ;  $v_{\text{turb}} = 280_{-80}^{+180} \text{ km s}^{-1}$ ; and  $v_{\text{shift}} = -607_{-342}^{+354} \text{ km s}^{-1}$ ), and absorber-2 ( $\log \xi = 3.3 \pm 0.2$ ;  $\log N_{\text{H}} = 22.1_{-0.2}^{+0.1} \text{ cm}^{-2}$ ;  $v_{\text{turb}} < 174 \text{ km s}^{-1}$ ; and  $v_{\text{shift}} = 213_{-158}^{+108} \text{ km s}^{-1}$ ), provides a better fit. Interestingly, for either scenario the Ar XVIII component cannot be modeled well unless the abundance of Ar is set to approximately twice solar. Table 2 lists ions detected in our spectrum, and also the strong lines that are predicted by our XSTAR models to have equivalent widths  $W_{\text{ion}} > 0.1 \text{ m\AA}$ , including three strong lines of Fe XXVI, Fe XXV, and Ca XX.

## 2.2. Orbital Phase Evolution of the H-like and He-like Fe Absorption

Given that the light curve (Figure 1) clearly indicates a blockage of the primary by the accretion stream and/or secondary, we next investigate relevant effects this might have on the observed ionized absorption. For this, we concentrate only on the evolution of the strongest absorption lines, i.e., Fe XXV and Fe XXVI, over the course of the 4U 1624–490  $\approx 76 \text{ ks}$  orbital period, as the source moves in and out of occultation. For this analysis, we use only the HEG given its higher resolution and throughput in this energy band.

### 2.2.1. Pre-dip versus Post-dip Phases Fe Line Changes

A simple overlay of the pre-dip (a+b;  $\approx 20 \text{ ks}$ ) and post-dip (d+e+f+g;  $\approx 38 \text{ ks}$ ) phases reveal nearly identical spectra. Our analysis here uses the blackbody plus power-law continuum (Section 2.1) and broad Fe emission line (Section 2.1.2) to model the more global features. While the underlying components are similar to that used for the time-averaged spectrum, the best-fit parameters differ slightly. To quantify this effect, we assess Fe line changes by adding Gaussians to model the Fe XXV and Fe XXVI absorption. The best-fit parameters (Table 3) do not indicate significant changes in absorption between the *pre-dip* and *post-dip* phases, so for these fits we do not proceed with the more involved XSTAR modeling.

### 2.2.2. Near-dip versus Far-dip Phases Fe Line Changes

Next, we considered a comparison between the *near-dip* (b+c+d;  $\approx 29 \text{ ks}$ ) and *far-dip*: (a+e+f+g;  $\approx 39 \text{ ks}$ ) spectra following (initially) the procedure of Section 2.2.1. Based on simple Gaussian fits, distinct Fe line changes are observed in the line parameters, most noticeably in the Fe XXV velocity width, equivalent width, and line flux (Figure 3 and Table 3). Figure 3 and Table 3 reveal distinct Fe absorption line changes with the Fe XXV:Fe XXVI flux ratios indicating noticeable plasma changes (temperature and ionization) between the *near-dip* and *far-dip* phases.

In an attempt toward a more physically realistic picture explaining these changes, we proceed with more rigorous photoionization modeling of these spectra. For this, we fixed the continuum parameters specific to each phase, and varied the XSTAR parameters as before to model the Fe XXV and Fe XXVI absorption features. For these spectra, we find that a single ionization absorber gives an overall reasonable fit in a  $\chi^2_{\nu}$  sense, but does not fully describe the Fe XXV absorption line. The fact

**Table 3**  
Best-fit Fe xxvi and Fe xxv Absorption Lines as Measured in the Different Phases

Orbital Phase	Wavelength (Å)(keV)	Width (mÅ)(km s <sup>-1</sup> )	EW (mÅ)	Line Flux	Wavelength (Å)(keV)	Width (mÅ)(km s <sup>-1</sup> )	EW (mÅ)	Line Flux
	Fe XXVI				Fe XXV			
Non-dip	1.778 <sup>+0.001</sup> <sub>-0.002</sub> (6.97)	5 <sup>+2</sup> <sub>-2</sub> (770 <sup>+383</sup> <sub>-358</sub> )	7.2 <sup>+1.3</sup> <sub>-1.5</sub>	4.4 <sup>+0.8</sup> <sub>-0.9</sub>	1.849 <sup>+0.007</sup> <sub>-0.004</sub> (6.71)	< 16.4 (< 2659)	3.1 <sup>+2.3</sup> <sub>-1.4</sub>	1.9 <sup>+1.4</sup> <sub>-0.8</sub>
Pre-dip	1.780 <sup>+0.003</sup> <sub>-0.003</sub> (6.97)	< 7.0 (< 1176)	5.5 <sup>+2.2</sup> <sub>-2.0</sub>	3.6 <sup>+1.4</sup> <sub>-1.3</sub>	1.848 <sup>+0.004</sup> <sub>-0.003</sub> (6.71)	< 10.0 (< 1623)	4.6 <sup>+2.3</sup> <sub>-2.0</sub>	3.0 <sup>+1.5</sup> <sub>-1.3</sub>
Post-dip	1.775 <sup>+0.003</sup> <sub>-0.002</sub> (6.97)	4 <sup>+3</sup> <sub>-3</sub> (758 <sup>+439</sup> <sub>-495</sub> )	6.0 <sup>+1.6</sup> <sub>-1.6</sub>	3.7 <sup>+1.0</sup> <sub>-1.0</sub>	1.858 <sup>+0.008</sup> <sub>-0.012</sub> (6.67)	12 <sup>+8</sup> <sub>-8</sub> (1934 <sup>+1295</sup> <sub>-1222</sub> )	4.5 <sup>+2.7</sup> <sub>-2.2</sub>	2.8 <sup>+1.7</sup> <sub>-1.3</sub>
Near-dip	1.778 <sup>+0.002</sup> <sub>-0.001</sub> (6.97)	< 3.8 (< 635)	5.1 <sup>+1.4</sup> <sub>-1.3</sub>	3.1 <sup>+0.9</sup> <sub>-0.8</sub>	1.857 <sup>+0.003</sup> <sub>-0.004</sub> (6.68)	7 <sup>+6</sup> <sub>-4</sub> (1171 <sup>+1049</sup> <sub>-571</sub> )	6.8 <sup>+2.6</sup> <sub>-2.1</sub>	4.1 <sup>+1.6</sup> <sub>-1.3</sub>
Far-dip	1.778 <sup>+0.002</sup> <sub>-0.003</sub> (6.97)	6 <sup>+3</sup> <sub>-3</sub> (1094 <sup>+492</sup> <sub>-427</sub> )	8.2 <sup>+1.9</sup> <sub>-1.8</sub>	5.0 <sup>+1.2</sup> <sub>-1.1</sub>	1.847 <sup>+0.001</sup> <sub>-0.002</sub> (6.71)	< 4.6 (< 746)	3.0 <sup>+1.1</sup> <sub>-1.2</sub>	1.9 <sup>+0.7</sup> <sub>-0.7</sub>

**Notes.** EW is the equivalent width, and the line flux is in units of  $10^{-4}$  ph cm<sup>-2</sup> s<sup>-1</sup>. Errors are quoted at 90% confidence.

that the relative Fe xxv and Fe xxvi velocity shifts are different in the far-dip and near-dip spectra (i.e., Figure 3) suggests that a more realistic physical model should consider two ionized absorbers arising from different physical regions. A fit to these near-dip and far-dip spectra using such a two-component ionized plasma: one hot ( $\approx 3.0 \times 10^6$  K corresponding to  $\log \xi \approx 4.2$ ) and another slightly cooler ( $\approx 1.0 \times 10^6$  K;  $\log \xi \approx 3.0$ ), gives a better description (Figure 3). By adding this second component, the  $\chi^2$  of the fit to the near-dip phases is reduced from 1047 for 1063 dof (one-component ionized plasma) to 1033 for 1059 dof (two-component ionized plasma). This yields an  $F$ -statistic value of 3.6, which for these four additional degrees of freedom formally corresponds to an improved fit at  $> 99\%$  confidence. (See, however, Protassov et al. (2002) for a discussion of the applicability of the  $F$ -test in situations such as those presented here.) We therefore view the two-component ionized plasma model as a more likely scenario for the 4U 1624–490 X-ray emitting regions.

### 2.2.3. Short Duration Changes

Since there is clear evidence for absorber changes when comparing the far- and near-dip periods, we conclude our analysis of the spectral variability by dividing the total persistent spectra into seven approximately equal duration parts of  $\approx 10$  ks each (Figures 1, 4, and 5). Of interest is whether the blackbody+power-law or partial coverer+power-law components vary with orbital phase. We first test for such variations by fitting our blackbody plus power-law continuum model, including the broad emission line and narrow Fe absorption lines. Figure 5(b) and (c) and Table 4 show that the unabsorbed fluxes of both the blackbody and power-law components, and to some extent the absorbed flux of the blackbody component, remain relatively steady over the 4U 1624–490 orbital period. The absorbed power-law component, however, is seen to vary more dramatically, and in a quasi-sinusoidal fashion ( $\approx 95\%$  confidence).

We note that the quasi-sinusoidal variation of the absorbed blackbody component is less than that of the absorbed power law, and perhaps exhibits an anticorrelation with the power law. We therefore assess the statistical correlation between these parameters by generating confidence contours for phase (g) (see Figures 4 and 5). These contours indicate a marked degree of dependence of the absorbed power-law and blackbody fluxes upon each other; therefore, in deriving a period for the modulation of the flux, we tie these two components together and fit a sine function to the points of Figure 5(c). Specifically, the power-law and blackbody fluxes are tied together, but the power-law flux is allowed a 1/2 period (delayed) phase shift. At 90% confidence, we derive a period  $T = 43_{-9}^{+13}$  ks ( $\approx 12$  hr), slightly more than half the orbital period.

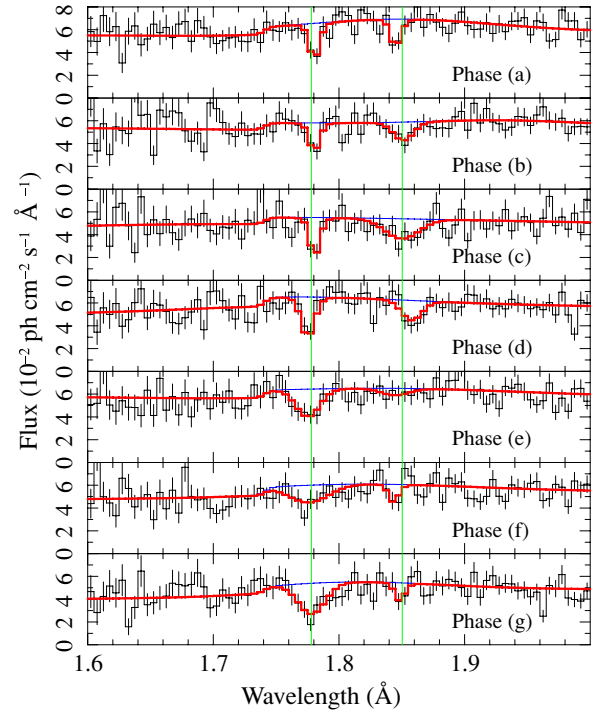


**Figure 4.** HEG spectra (black) and best-fit model (red) showing the evolution of the Fe xxv and Fe xxvi absorption lines over the 4U 1624–490 orbital period. As in Figure 3, the vertical green lines indicate the laboratory wavelengths of Fe xxv (1.850 Å) and Fe xxvi (1.778 Å).

Next, we explore the time dependence of the partial covering model (see the description in Section 2.1.1) by fitting simultaneously the seven phased spectra. We wish to determine whether the change of the absorbed power-law flux is produced by variation of the local cold gas. Here we tie together all fit parameters (including power-law normalization and slope), but allow the partial covering fraction and local absorption, i.e., the cold absorption along the line of sight, to vary with orbital phase. We find that this model describes the seven phased spectra well, giving  $\chi^2$  of 5971 for 5896 dof and yields values of  $N_H = 9.11_{-0.24}^{+0.23} \times 10^{22}$  cm<sup>-2</sup> and  $\Gamma = 2.26_{-0.05}^{+0.06}$ . Figure 6 shows that the equivalent hydrogen column density of the local cold absorber varies significantly over the orbital phase, while the partial covering factor remains relatively steady. This variation of the hydrogen column density of the local cold absorber is very similar to the phase-dependent variations seen for the absorbed power-law flux in the alternative blackbody+power-law models described above; therefore, we also use a sine function to fit the points of Figure 6(c). At 90% confidence, we derive a period  $T = 47 \pm 7$  ks, similar to the fits above. Again, we

**Table 4**  
Best-Fit Parameters Over  $\sim 10$  ks Time Step

Phase	$N_{\text{H}}$ ( $10^{22} \text{ cm}^{-2}$ )	kT (keV)	uFlux	Flux	$\Gamma$	uFlux	Flux	$E$ (KeV) (Å)	Width (KeV) ( $10^3 \text{ km s}^{-1}$ )	Flux	
			Blackbody			Power law			Fe Emission Feature		
a	$7.6^{+0.7}_{-0.4}$	$1.35^{+0.09}_{-0.05}$	$11.7^{+1.1}_{-2.2}$	$6.4^{+0.5}_{-1.3}$	$0.8^{+0.7}_{-0.8}$	$7.7^{+4.5}_{-3.4}$	$4.9^{+1.3}_{-0.8}$	$6.67^{+0.12}_{-0.08}$ (1.858)	$0.25^{+0.08}_{-0.11}$ ( $11^{+4}_{-5}$ )	$1.7^{+0.5}_{-0.5}$	
b	$7.3^{+1.0}_{-0.3}$	$1.32^{+0.07}_{-0.06}$	$11.3^{+1.6}_{-3.0}$	$6.2^{+0.9}_{-1.8}$	$0.5^{+0.9}_{-0.5}$	$6.5^{+5.7}_{-2.0}$	$4.5^{+2.0}_{-1.1}$	$6.44^{+0.41}_{-0.25}$ (1.925)	$< 0.8$ ( $< 37$ )	$0.4^{+0.5}_{-0.4}$	
c	$7.4^{+0.4}_{-0.3}$	$1.46^{+0.12}_{-0.11}$	$12.0^{+2.4}_{-2.2}$	$6.8^{+1.3}_{-1.4}$	$1.0^{+1.3}_{-1.0}$	$4.1^{+4.6}_{-1.6}$	$2.5^{+1.6}_{-1.6}$	$6.96^{+1.01}_{-0.28}$ (1.781)	$0.19^{+0.60}_{-0.22}$ ( $49^{+151}_{-46}$ )	$0.6^{+0.7}_{-0.5}$	
d	$8.0^{+1.4}_{-0.9}$	$1.48^{+0.12}_{-0.11}$	$12.6^{+1.0}_{-2.2}$	$6.9^{+0.5}_{-1.3}$	$1.7^{+1.1}_{-1.4}$	$8.6^{+13.9}_{-5.9}$	$3.5^{+1.5}_{-0.8}$	$6.91^{+0.19}_{-0.16}$ (1.794)	$0.30^{+0.19}_{-0.14}$ ( $13^{+8}_{-6}$ )	$1.6^{+0.8}_{-0.7}$	
e	$7.4^{+0.6}_{-0.3}$	$1.32^{+0.08}_{-0.06}$	$11.2^{+2.9}_{-1.8}$	$6.1^{+0.7}_{-1.5}$	$0.7^{+0.7}_{-0.7}$	$7.8^{+5.0}_{-2.9}$	$5.2^{+1.6}_{-0.8}$	$6.58^{+0.18}_{-0.19}$ (1.884)	$0.21^{+0.25}_{-0.11}$ ( $10^{+11}_{-5}$ )	$1.0^{+0.7}_{-0.7}$	
f	$7.6^{+1.2}_{-0.6}$	$1.31^{+0.14}_{-0.05}$	$11.7^{+1.3}_{-1.6}$	$6.3^{+0.7}_{-0.9}$	$1.1^{+1.1}_{-1.5}$	$6.8^{+7.4}_{-5.1}$	$3.8^{+1.1}_{-0.8}$	$6.69^{+0.23}_{-0.22}$ (1.853)	$0.28^{+0.41}_{-0.17}$ ( $13^{+18}_{-8}$ )	$1.0^{+0.6}_{-0.5}$	
g	$7.7^{+0.7}_{-0.5}$	$1.26^{+0.06}_{-0.05}$	$11.8^{+1.7}_{-1.6}$	$6.2^{+0.9}_{-1.0}$	$1.1^{+0.8}_{-1.1}$	$5.5^{+4.5}_{-3.1}$	$3.2^{+1.0}_{-1.1}$	$6.82^{+0.34}_{-0.14}$ (1.818)	$0.26^{+0.29}_{-0.12}$ ( $11^{+12}_{-5}$ )	$1.4^{+1.3}_{-0.6}$	

**Notes.**  $N_{\text{H}}$  is the LOS cold hydrogen column density. uFlux and Flux refer respectively to the unabsorbed and absorbed integrated flux ( $10^{-10} \text{ erg cm}^{-2} \text{ s}^{-1}$ ) over 0.6–10.0 keV.  $I_{\text{line}}$  is the flux ( $10^{-2} \text{ ph cm}^{-2} \text{ s}^{-1}$ ) of the broad Fe emission line. Errors are quoted at 90% confidence.

**Table 5**  
Best-Fit Parameters of Fe H-Like and He-Like Absorption Lines

Phase	Wavelength (Å)(keV)	Width (mÅ)( $\text{km s}^{-1}$ )	EW (mÅ)	Flux	Wavelength (Å)(keV)	Width (mÅ)( $\text{km s}^{-1}$ )	EW (mÅ)	Flux
	Fe XXVI				Fe XXV			
a	$1.780^{+0.003}_{-0.002}$ (6.97)	$< 7.4 (< 1250)$	$5.9^{+1.7}_{-2.0}$	$4.1^{+1.2}_{-1.4}$	$1.845^{+0.003}_{-0.002}$ (6.72)	$< 6.2 (< 1006)$	$4.7^{+1.8}_{-2.1}$	$3.2^{+1.2}_{-1.4}$
b	$1.780^{+0.003}_{-0.003}$ (6.97)	$< 6.2 (< 1042)$	$5.0^{+1.8}_{-2.2}$	$3.2^{+1.2}_{-1.4}$	$1.852^{+0.010}_{-0.006}$ (6.69)	$< 20.6 (< 3342)$	$6.0^{+4.4}_{-3.4}$	$3.8^{+2.8}_{-2.2}$
c	$1.782^{+0.001}_{-0.002}$ (6.96)	$< 4.4 (< 749)$	$7.8^{+1.9}_{-2.5}$	$4.2^{+1.0}_{-1.3}$	$1.850^{+0.007}_{-0.010}$ (6.70)	$13^{+7}_{-7}$ ( $2077^{+1166}_{-1061}$ )	$13.1^{+7.0}_{-5.6}$	$7.1^{+3.8}_{-3.0}$
d	$1.775^{+0.003}_{-0.002}$ (6.99)	$< 3.9 (< 667)$	$5.9^{+1.8}_{-2.2}$	$3.9^{+1.2}_{-1.4}$	$1.860^{+0.000}_{-0.004}$ (6.67)	$< 6.9 (< 1110)$	$5.7^{+1.9}_{-2.2}$	$3.8^{+1.2}_{-1.4}$
e	$1.776^{+0.004}_{-0.005}$ (6.98)	$8^{+5}_{-4}$ ( $1377^{+878}_{-648}$ )	$10.4^{+3.9}_{-3.2}$	$6.7^{+2.5}_{-2.1}$	$1.845^{+0.015}_{-0.005}$ (6.72)	$< 10.0 (< 1626)$	$< 6.5$	$< 4.2$
f	$1.777^{+0.010}_{-0.007}$ (6.98)	$< 15.0 (< 2532)$	$11.6^{+4.2}_{-4.6}$	$7.1^{+2.5}_{-2.8}$	$1.845^{+0.003}_{-0.005}$ (6.72)	$< 4.9 (< 803)$	$3.3^{+2.2}_{-2.4}$	$2.0^{+1.3}_{-1.5}$
g	$1.780^{+0.006}_{-0.005}$ (6.97)	$9.6^{+5.7}_{-5.3}$ ( $2028^{+1161}_{-1112}$ )	$14.5^{+5.5}_{-5.3}$	$8.3^{+3.1}_{-3.0}$	$1.850^{+0.003}_{-0.005}$ (6.70)	$< 7.5 (< 1218)$	$3.8^{+2.2}_{-2.7}$	$2.2^{+1.3}_{-1.5}$

**Notes.** EW is the equivalent width and the unit of flux is  $10^{-4} \text{ ph cm}^{-2} \text{ s}^{-1}$ . Errors are quoted at 90% confidence.

**Table 6**  
Best-Fit Parameters from XSTAR Photoionization Models of the Near-Dip and Far-Dip Phases

Phase	$\log(\xi)$ ( $\text{erg cm s}^{-1}$ )	$\log(N_{\text{H}})$ ( $\text{cm}^{-2}$ )	$v$ ( $\text{km s}^{-1}$ )	$\log(\xi)$ ( $\text{erg cm s}^{-1}$ )	$\log(N_{\text{H}})$ ( $\text{cm}^{-2}$ )	$v$ ( $\text{km s}^{-1}$ )
	Hot Absorption			Warm Absorption		
Near-dip	$4.2^{+0.8}_{-0.6}$	$23.4^{+0.5}_{-0.6}$	$335^{+346}_{-318}$	$3.1^{+0.2}_{-0.2}$	$22.3^{+0.3}_{-0.4}$	$-276^{+271}_{-172}$
Far-dip	$4.3^{+0.7}_{-0.6}$	$23.3^{+0.3}_{-0.3}$	$-263^{+306}_{-310}$	$3.4^{+0.2}_{-0.1}$	$22.2^{+0.2}_{-0.2}$	$1028^{+4890}_{-307}$

**Notes.**  $\xi$  is the photoionization parameter from XSTAR. “ $N_{\text{H}}$ ” is the equivalent hydrogen column density in the associated ionized region. “ $v$ ” is the measured velocity shift, (–) blueshift toward us and (+) redshift away from us. Errors are quoted at 90% confidence.

are seeing evidence that the observed orbital modulations are predominantly driven by absorption variations, rather than by intrinsic source variations, regardless of whether we fit a blackbody plus power-law model, or instead fit a partial covering model of a single component (i.e., the power law).

We also investigate Fe xxv and Fe xxvi absorption line changes over these smaller time segments by fitting Gaussian lines to the absorption features while fixing the continuum parameters to the phase-specific values of Table 4. (Here, the HEG spectrum is binned to  $0.005 \text{ Å bin}^{-1}$ .) Table 5 and Figures 4, and 5(IV) show that the Fe xxvi velocity width is narrowest during phases c and d that occur immediately after dipping events. In contrast, it appears that it is the Fe xxv flux and velocity shift that change most dramatically over the orbital

period, supporting our interpretation that these lines originate in different regions (see Section 3). This result is consistent with the findings from previous sections (see, e.g., Table 6) whereby a comparison between XSTAR modeling of the near-dip and far-dip regions show that the largest changes come from the less-ionized “warm” region of  $\log \xi \approx 3$ .

### 3. DISCUSSION

Our *Chandra*-HETGS spectral study of 4U 1624–490 over its orbital period confirms the detection of H- and He-like Fe xxv and Fe xxvi absorption. Detailed photoionization modeling with XSTAR predicts additional lines from Ca xx, Ar xvii, and S xvi. Of particular note is not only the confirmation of these lines with



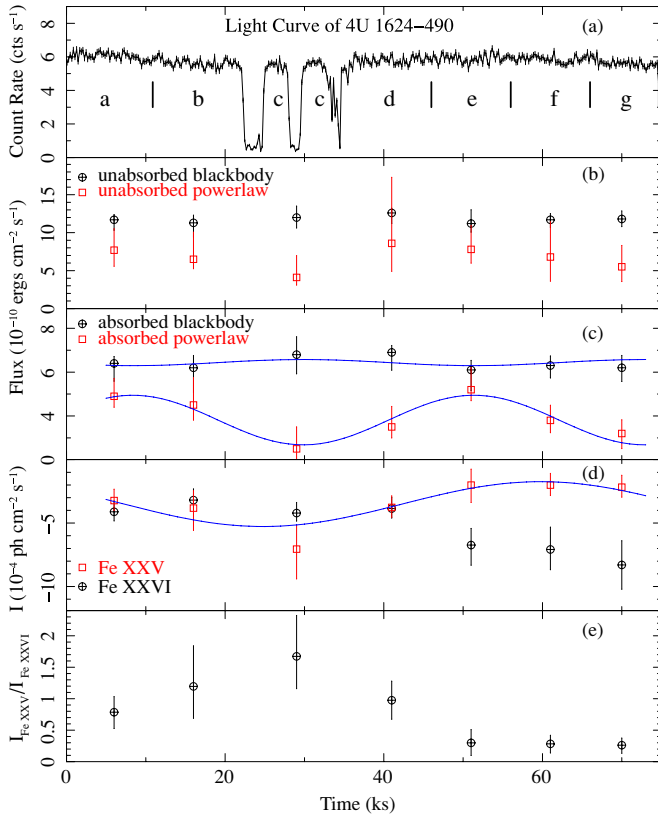


**Figure 5.** (a) Tracking the 4U 1624–490 light curve over 10 ks time steps shows that the unabsorbed fluxes of both the blackbody and power-law components (b), and to a lesser extent the absorbed flux of the blackbody component (c), remain relatively steady, whereas the absorbed power-law component (c) reaches a minimum during the periods near dipping events. Both components can be described by sine waves (blue curves). (d) Intensity evolution of the Fe absorption lines. The blue curve is also a sine wave fitting to the intensity of Fe XXV absorption line. (e) The evolution of the intensity ratio of the absorption lines shows a quasi-sinusoidal variation. In this figure only, all error bars shown are at the  $1\sigma$  confidence level. The vertical bars in subfigure (a) indicate the different phases of flux evolution.

detailed photoionization modeling, but also that the variability analysis strongly suggests that these lines can be identified as originating from the accretion disk corona (dominated by high ionization plasma giving rise predominantly to Fe XXVI) and the outer accretion disk (as indicated by the flux evolution of the lower ionization variable Fe XXV absorption).

While the time-averaged spectrum over the 4U 1624–490 orbital period can be modeled reasonably well with one ionization zone, variability studies instead suggest that a model with two ionization zones is a better description of the data. This interpretation has important implications for geometric scenarios and our ability to map the emitting regions as a function of orbital phase. In an earlier analysis of this data set, Iaria et al. (2007) claimed velocity widths of up to  $3500 \text{ km s}^{-1}$ , to which they attribute an origin between the external region of the ADC and the disk edge. In this interpretation, the broadening would be due to bulk motion or turbulence connected to the coronal activity. Our variability results indicate that neither bulk motion nor turbulence is necessary to produce the line widths. We arrive at this conclusion based on variability studies where line velocity widths are seen to change over relatively short timescales, and that in some phases the velocity widths are comparable to the HEG FWHM resolution (i.e., Fe XXVI during the near-dip phase, and Fe XXV during the far-dip phase) and therefore are easily described by thermal broadening.

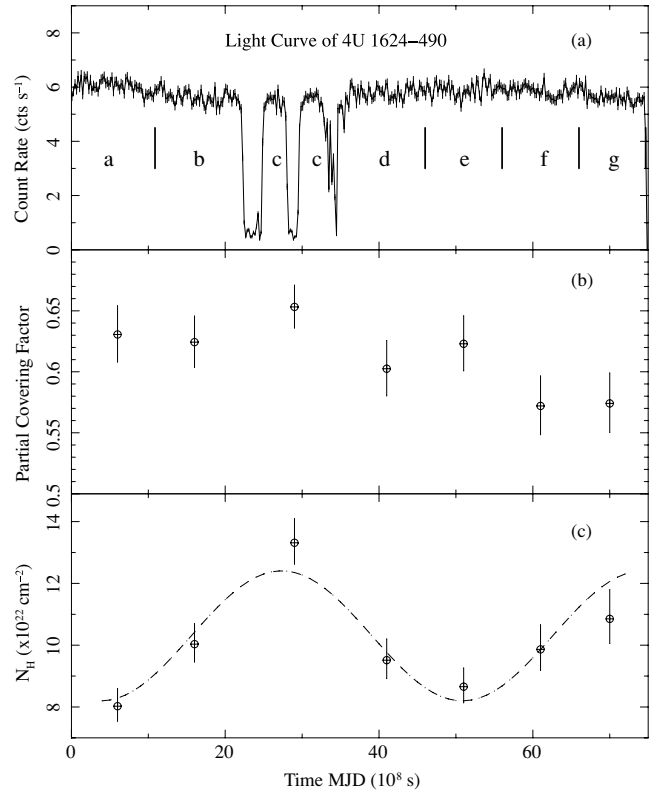


**Figure 6.** Evolution of (b) the partial covering factor and (c) the equivalent hydrogen column density of the local absorber, which reaches a maximum during the periods near dipping events. Similar to the fits in Figure 5, the equivalent hydrogen column density also can be described by a sine wave with a period of  $T = 47 \pm 7 \text{ ks}$  (dashed curve). In this figure, all error bars shown are at the  $1\sigma$  confidence level.

To take our two-region model further, we consider it in the context of simple arguments relating the ionization parameter to the location of the absorbing plasma. As pointed out by Tarter et al. (1969), the ionization parameter  $\xi$  can be defined by the relation  $\xi = L_X n_e^{-1} R^{-2}$ , where  $L_X$  is the total un-absorbed source luminosity ( $= 4.9 \times 10^{37} \text{ erg s}^{-1}$  between 1 and 10 keV during the epoch of our 4U 1624–490 observation) and  $R$  is the distance to the absorbing plasma. The electron particle density  $n_e = N_H/\Delta R$  is characterized by the thickness of the absorbing medium,  $\Delta R$ , and the equivalent Hydrogen column of the ionized region. Using this, we consider the possible range of  $R$  for the plasma giving rise to the observed ionized absorption lines.

A sketch of a scenario explaining the major results of such an analysis is shown in Figure 7. As discussed above, the observed orbital variability of the different spectral components points toward an extended ADC similar to the emission geometry proposed by White et al. (1988) or Church & Balucińska-Church (2004; see Church 2004 for a summary). In this model, the ADC is large and therefore only slight variations of its components with orbital phase are expected, in line with our observation that the hot plasma component is constant over the orbit. This location of the hot component is consistent with the spectral analysis: our modeling efforts show that the “hot” gas component can be described by  $\xi_{\text{hot}} \approx 10^{4.3} \text{ erg cm s}^{-1}$  ( $T \approx 3 \times 10^6 \text{ K}$ ) ionizing a plasma of column  $\approx 2 \times 10^{23} \text{ cm}^{-2}$ . “Naively” assuming a geometrically thick  $\Delta R \sim R$ , a distance  $R \sim 3 \times 10^{10} \text{ cm}$  is obtained, which is comparable to the size

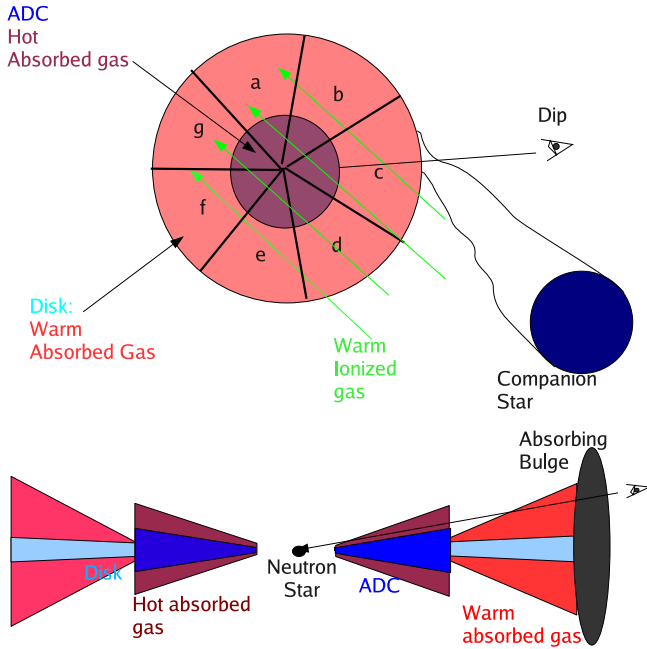


**Figure 7.** 4U 1624–490 geometry in the context of our line-of-sight view as determined from absorption line variability studies. Our studies indicate that the hotter component dominates the ADC, whereas the cooler gas is associated with the outer disk rim, which intersects our line of sight. a–g refer to the 4U 1624–490 orbital phase as indicated by the light curve of Figure 1(a).

of the ADC derived from the relation  $R_{\text{ADC}} = L_X^{0.88 \pm 0.16}$  of Church & Balucińska-Church (2004). A similar value for an extended ADC was recently determined by Schulz et al. (2009) while measuring Doppler broadening in several broad emission lines in Cygnus X-2.

In contrast,  $\xi_{\text{warm}}$  changes more dramatically over the 4U 1624–490 orbital phase with the largest differences seen in a comparison between the far-dip ( $\xi \approx 10^{3.4}$  erg cm s<sup>-1</sup>;  $T \approx 1.0 \times 10^6$  K) and near-dip ( $\xi \approx 10^{3.1}$  erg cm s<sup>-1</sup>;  $T \approx 0.9 \times 10^6$  K) phases. This component cannot originate in the ADC: If one assumes  $\Delta R \sim R$  and a column density of  $N_{\text{H}} \approx 2 \times 10^{22}$  cm<sup>-2</sup> as appropriate for the “warm” component (Table 6), the data require  $R \sim 10^{12}$  cm, which is significantly larger than the likely accretion disk radius of  $\sim 10^{11}$  cm. If, however, a geometrically thin plasma of  $\Delta R/R \sim 0.1$  is assumed for this “warm” component, absorber distances between  $1.8 \times 10^{11}$  cm (near-dip) and  $\approx 1.1 \times 10^{11}$  cm (far-dip) are obtained. Since the radius of the accretion disk is  $\approx 1.1 \times 10^{11}$  cm as obtained from the Roche Lobe size of the neutron star (Church & Balucińska-Church 2004), it is therefore likely that the warm component originates in the accretion disk rim, e.g., where the accretion stream impacts onto the disk and where gas is irradiated by the neutron star.

We note that this interpretation of the absorbers is also consistent with the variation of the broadband spectral parameters shown in Figure 5. In terms of the model of White et al. (1988) and Church & Balucińska-Church (2004), the blackbody component is taken to originate from the neutron star, while the power-law component is interpreted as being due to Comptonization in the extended ADC. In this interpretation, the power-law component is expected to exhibit a quasi-sinusoidal variation and to be weakest during the times of dipping when the ADC is partly covered by the warm absorbing material. A consequence of this model is also that the ratio Fe xxv/Fe xxvi

shows a maximum during the dipping, since the optical depth in Fe xxv is largest during that time.

We also note that the evolution of the spectrum can be modeled with partial covering of a single power-law component, with the local absorber varying over orbital phase. In such a model, the soft-end of the uncovered power-law replaces the blackbody component. This offers a slightly different explanation of the relative strength of the variation of the absorbed power-law component, relative to the blackbody. The “covered power-law” is that portion of the ADC at low latitudes, where obscuration by the disk is expected to be greatest, and the ADC is expected to be widest. The “uncovered power-law” arises from a geometrically narrower region at high latitudes, where obscuration by the disk is the least. For either the blackbody plus power-law scenario, or the partial covering scenario, our analysis shows that variations are predominantly driven by changes in obscuration, rather than any intrinsic variation of the components.

#### 4. SUMMARY

We summarize the major conclusions and discoveries of this paper:

1. A reanalysis of the *Chandra*-HETGS spectrum of 4U 1624–490 based on photoionization modeling and variability studies shows that while the continuum spectrum can be modeled using a blackbody plus power law, a slightly more preferred model is a single  $\Gamma = 2.25$  power-law partially (71%) covered by a local absorber of column density  $N_{\text{H, Local}} = 8.1^{+0.7}_{-0.6} \times 10^{22}$  cm<sup>-2</sup>. The total  $1.6 \times 10^{23}$  cm<sup>-2</sup> large line of sight ( $N_{\text{H, Local}} + N_{\text{H, Gal}}$ ) column therefore can attenuate the power law up to 5 keV, even though the X-ray spectrum can be seen down to 1.7 keV. For spectra with limited (e.g., 0.5–10 keV) band coverage, the severe absorption at the low energies coupled with limited counts at the high energies can flatten a  $\Gamma = 2.25$  power-law to appear as  $\Gamma \sim 1.2$ . The source luminosity at the epoch of our observations is estimated to be  $4.9 \times 10^{37}$  erg s<sup>-1</sup> for a distance of 15 kpc as recently determined by Xiang et al. (2007).
2. We report the discovery of a possible quasi-sinusoidal modulation with period  $P = 43^{+13}_{-9}$  ks over the  $\sim 76$  ks orbital period, with the caveat that we have observed 4U 1624–490 only over one binary orbit. There is strong indication that variations in observed spectral properties are predominantly driven by changes in obscuration, rather than any intrinsic variation of the power-law or black-body components.
3. We confirm the detection of ionized absorption from Fe xxvi, Fe xxv, and Ca xx, which have been detected by Iaria et al. (2007). *Detailed photoionization modeling with XSTAR has allowed us to derive the strengths of other absorption lines of Mg, Si, S and Ar.*
4. Our detailed variability studies of detected strong absorption lines point to a two-temperature plasma for their origin: a highly ionized component of  $\xi_{\text{hot}} \approx 10^{4.3}$  erg cm s<sup>-1</sup> ( $T \sim 3.0 \times 10^6$  K) associated with an extended accretion disk corona of  $R \sim 3 \times 10^{10}$  cm, and a less ionized more variable component of  $\xi \approx 10^{3.4}$  erg cm s<sup>-1</sup> ( $T \sim 1.0 \times 10^6$  K; far-dip) and  $\xi \approx 10^{3.1}$  erg cm s<sup>-1</sup> ( $T \sim 9.0 \times 10^5$  K; near-dip) coincident with the accretion disk rim. This model is offered in favor of bulk Comptonization, as previously suggested, as an explanation for observed line broadening.

5. We also report Fe xxv and Fe xxvi absorption line variations (in wavelength, strength, width) over the 4U 1624–490 orbital period. This, with previously noted variations have allowed us to map plasma properties to our viewing of 4U 1624–490 over its  $\sim 76$  ks orbital period (see Figure 7).

This work was funded by the NASA/*Chandra* grant GO4-3056X; we are thankful for its support. J.C.L. thanks the Harvard University Faculty of Arts and Sciences for supplemental financial support.

## REFERENCES

- Angelini, L., Parmar, A., & White, N. 1997, in ASP Conf. Ser 121, IAU Colloquium 163, ed. D. T. Wickramasinghe, G. V. Bicknell, & L. Ferrario (San Francisco, CA: ASP), 685
- Arnaud, K. A. 1996, ASPC, 101, 17
- Asai, K., Dotani, T., Nagase, F., & Mitsuda, K. 2000, *ApJS*, 131, 571
- Balucińska-Church, M., Barnard, R., Church, M. J., & Smale, A. P. 2001, *A&A*, 378, 847
- Balucińska-Church, M., Humphrey, P. J., Church, M. J., & Parmar, A. N. 2000, *A&A*, 360, 583
- Balucińska-Church, M., & McCammon, D. 1992, *ApJ*, 400, 699
- Canizares, C. R., et al. 2005, *PASP*, 117, 1144
- Church, M. J., *RevMexAA*, 20, 140
- Church, M. J., & Balucińska-Church, M. 1995, *A&A*, 300, 441
- Church, M. J., & Balucińska-Church, M. 2004, *MNRAS*, 348, 955
- Christian, D. J., & Swank, J. H. 1997, *ApJS*, 109, 177
- Díaz-Trigo, M., Parmar, A. N., Boirin, L., Méndez, M., & Kaastra, J. S. 2006, *A&A*, 445, 179
- Grevesse, N., Noels, A., & Sauval, A. J. 1996, *Cosmic Abundances*, 99, 117
- Hirano, T., Hayakawa, S., Nagase, F., Masai, K., & Mitsuda, K. 1987, *PASJ*, 39, 619
- Houck, J. C., & Denicola, L. A. 2000, in ASP Conf. Proc. 216, *Astronomical Data Analysis Software and Systems IX*, ed. N. Manset, C. Veillet, & D. Crabtree (San Francisco, CA: ASP), 591
- Iaria, R. L., D’Aí, G., Di Salvo, R., & Robba, N. R. 2007, *A&A*, 463, 289
- Jones, M. H., & Watson, M. G. 1989, in Proc. 23rd ESLAB Symp. ed. J. Hunt & B. Battrick (ESA SP-296, Noordwijk: ESA), 439
- Juett, A. M., & Charkabarty, D. 2006, *ApJ*, 646, 493
- Kallman, T. 2005, *AAS*, 206, 3124
- Lee, J. C., Reynolds, C. S., Remillard, R., Schulz, N. S., Blackman, E. G., & Fabian, A. C. 2002, *ApJ*, 567, 1102
- Lommen, D., van Straaten, S., van der Klis, M., & Anthonisse, B. 2005, *A&A*, 435, 1005
- Neilsen, J., & Lee, J. C. 2009, *Nature*, 458, 481
- Noble, M. S., & Nowak, M. A. 2008, *PASP*, 120, 821
- Parmar, A. N., Oosterbroek, T., Boirin, L., & Lumb, D. 2002, *A&A*, 386, 910
- Protassov, R., van Dyk, D. A., Connors, A., Kashyap, V. L., & Siemiginowska, A. 2002, *ApJ*, 571, 545
- Schulz, N. S., Huenemoerder, D. P., Ji, L., Nowak, M., Yao, Y., & Canizares, C. R. 2009, *ApJ*, 692, L80
- Smale, A. P., Church, M. J., & Balucińska-Church, M. 2001, *ApJ*, 550, 962
- Suzuki, K., Matsuoka, M., Inoue, H., Mitsuda, K., Tanaka, Y., Ohashi, T., Hirano, T., & Miyamoto, S. 1984, *PASJ*, 36, 761
- Tarter, C. B., Tucker, W. H., & Salpeter, E. E. 1969, *ApJ*, 156, 943
- Wachter, S., Wellhouse, J. W., Patel, S. K., Smale, A. P., Alves, J. F., & Bouchet, P. 2005, *ApJ*, 621, 393
- Watson, M. G., Willingale, R., King, A. R., Gringdlay, J. E., & Halpern, J. 1985, *Space Sci. Rev.*, 40, 195
- White, N. E., Peacock, A., Hasinger, G., Mason, K. O., Manzo, G., Taylor, B. G., & Branduardi-Raymont, G. 1986, *MNRAS*, 218, 129
- White, N., Stella, L., & Parmar, A. 1988, *ApJ*, 324, 363
- Wilms, J., Allen, A., & McCray, R. 2000, *ApJ*, 542, 914
- Xiang, J. G., Lee, J. C., & Nowak, M. A. 2007, *ApJ*, 660, 1309